PROCEEDINGS OF SCIENCE

On the statistical characterization of the synchrotron multi-zone polarization of blazars

A. Tramacere[a,*]

[a] *Department of Astronomy, University of Geneva, Ch. d'Ecogia 16, 1290 Versoix, Switzerland*

E-mail: andrea.tramacere@unige.ch, andrea.tramacere@gmail.com

Polarimetric observations across multiple wavelengths reveal that blazars exhibit complex, energy-dependent polarization behavior, marked by a systematic decline in polarization fraction from X-rays to millimeter bands and pronounced variability in the electric vector position angle (EVPA). Such behavior defies the predictions of simple, single-zone synchrotron models and points instead to a highly turbulent jet environment composed of multiple, spatially distinct emission zones.

We present a statistical framework designed to interpret these energy-dependent polarization patterns, with particular emphasis on X-ray measurements from IXPE and optical observations from RoboPol. Employing a Monte Carlo approach implemented with the `JetSeT` code, we simulate synchrotron emission from a spherical region populated by turbulent cells with randomly distributed physical properties. The model explores a broad parameter space, including configurations with identical cells as well as systems following power-law distributions in both cell size and the parameters of the electron energy distribution (EED).

Our results demonstrate that the observed polarization trends can be fully accounted for by a purely turbulent, multi-zone model, without requiring correlations between the cell size and the EED parameters. The polarization degree is primarily governed by the effective number of flux-weighted emitting cells, which depends sensitively on the dispersion of cell properties—especially the EED cutoff energy at high frequencies and the low-energy spectral index at low frequencies. Adopting a fractional dispersion of the order of 90% in the EED cutoff energy and a low-energy spectral index dispersion of $\approx 0.5 - 1.5$, the model successfully reproduces both the millimeter-to-X-ray polarization evolution observed in IXPE multiwavelength campaigns and the optical polarization limiting envelope revealed by RoboPol observations.

39th International Cosmic Ray Conference (ICRC2025)
15–24 July 2025
Geneva, Switzerland

*Speaker

PoS(ICRC2025)868

1. Introduction

Blazars are active galactic nuclei (AGN) with relativistic jets aligned close to our line of sight, producing highly beamed, variable, and polarized emission across the electromagnetic spectrum [4]. Their spectral energy distributions (SEDs) exhibit two principal components: a low-energy component, interpreted as synchrotron (S) radiation emitted by ultrarelativistic electrons, peaking from the infrared (IR) to the X-ray band, and a high-energy component, which peaks in the γ-rays, attributed either to inverse Compton (IC) emission in purely leptonic models [3] or to high-energy emission from ultrarelativistic protons in hadronic models[5]. These sources are traditionally classified based on their S peak frequency (ν_p^S), ranging from low S peaked (LSP, $\nu_p^S < 10^{14}$ Hz) through intermediate S peaked (ISP, $10^{14} < \nu_p^S < 10^{15}$ Hz) to high S peaked (HSP, $\nu_p^S > 10^{15}$ Hz) blazars. [1]. The S component is linearly polarized, with polarization fraction rising from near zero at millimeter frequencies to tens of percent above the SED peak [10]. RoboPol observations [2] revealed that the fractional optical polarization depends on ν_p^S, showing a limiting envelope, with both the polarization and its dispersion, higher in LSP sources than in HSPs. They also demonstrated that the randomness of the optical electric vector position angle (EVPA) is higher in LSP objects compared to HSP sources. Recent advances, especially with Imaging X-ray Polarimetry Explorer (IXPE) [18], have enabled X-ray polarization measurements in blazars [6, 7, 9, 18], showing X-ray polarization degrees of 10–20% that decrease at lower frequencies, with optical polarization exceeding that at mm frequencies. Here, we summarize the key results presented in [15], based on a Monte Carlo multi-zone synchrotron framework modeling turbulent jet regions with power-law cell size distributions and variable electron cutoff energies. The approach statistically constrains cell properties needed to reproduce the multiwavelength polarization behavior of blazars observed by IXPE (HSPs) and RoboPol (optical).

2. Synchrotron Polarization

Let us consider a single, homogeneous spherical emitting region permeated by an ordered magnetic field B, and populated by relativistic electrons described by an energy distribution (EED) $n(\gamma)$. According to the standard synchrotron theory [11, 19], the degree of linear polarization is given by the flux emitted in the directions parallel ($F_{\nu,\parallel}$) and perpendicular ($F_{\nu,\perp}$) to the projection of the magnetic field on the plane of the sky: $\Pi_\nu^{\rm ord} = \frac{F_\nu^{\rm pol}}{F_\nu} = \frac{F_{\nu,\perp}-F_{\nu,\parallel}}{F_{\nu,\perp}+F_{\nu,\parallel}} = \frac{\int G(\nu/\nu_c)n(\gamma)d\gamma}{\int F(\nu/\nu_c)n(\gamma)d\gamma}$ where ν_c is the S critical frequency and the functions $F(x) \equiv x\int K_{5/3}(\xi)d\xi$ and $G(x) \equiv xK_{2/3}(x)$, are defined in terms of modified Bessel functions of the second kind and fractional order. The computation of the S emission, both for the SED emitted flux and polarization, is performed using the `JetSeT`[1] framework `v1.3.1` [14, 16, 17]. If we define a reference direction on the plane of the sky, and χ is the angle between this direction and the projection of the magnetic field on the plane of the sky, then $\Pi_\nu^{\rm ord}$ can be expressed in terms of Stokes' parameters:$\Pi_\nu^{\rm ord} = \frac{\sqrt{(U_\nu^2+Q_\nu^2)}}{F_\nu} = \frac{F_\nu^{\rm pol}\sqrt{\sin(2\chi)^2+\cos(2\chi)^2}}{F_\nu}$ .For a power-law EED :$\Pi(p) = \frac{p+1}{p+7/3}$. The relation above holds only for a pure power-law EED, or when the S emission is dominated by the power-law branch of the underlying EED. Now, let's consider a system of N_c cells, with $N_\nu \leq N_c$ indicating the number of cells emitting at the frequency ν. In

[1] https://github.com/andreatramacere/jetset https://jetset.readthedocs.io/en/latest/index.html

each cell, the magnetic field is ordered, but the single cell position angle, χ_i^r is randomly oriented, and $F_{\nu,i}$ is the single cell flux. For the specific case of almost identical cells, i.e. $F_{\nu,i} \approx \bar{F}_\nu$, and $F_{\nu,i}^{\rm pol} \approx \bar{F}_\nu^{\rm pol}$, the average degree of the linear S polarization ($\langle\Pi_\nu\rangle$), at a given frequency, can be evaluated as in [10]: $\langle\Pi_\nu\rangle = \Pi_\nu^{\rm ord}\bar{F}_\nu < \frac{\sqrt{(\sum_i^{N_\nu}\sin(2\chi_i^r))^2+(\sum_i^{N_\nu}\cos(2\chi_i^r))^2}}{\sum_i^{N_\nu}\bar{F}_\nu} >\approx \frac{\Pi_\nu^{\rm ord}}{\sqrt{N_\nu}}$ We can also define a depolarization factor, as in [10]: $\kappa_\nu = \sqrt{f_{\rm ord}^2 + \frac{(1-f_{\rm ord})^2}{N_\nu}}$ where $f_{\rm ord}$ is the fraction of the coherent magnetic field in the system, which reduces to $\kappa_\nu = \frac{1}{\sqrt{N_\nu}}$, for $f_{\rm ord} = 0$. In the following we will investigate on the case of $f_{\rm ord} = 0$, so all the results presented in the following can be easily rescaled to the case of $0 < f_{\rm ord} \leq 1$. In a more general and realistic scenario, the flux of each cell,$F_{\nu,i}$, will depend on the the physical properties of each cell, i.e. $F_{\nu,i} \neq \bar{F}_\nu$, preventing from factoring out the F_ν term:

$$\Pi_\nu = \frac{\sqrt{(\sum_i^{N_\nu} F_{\nu,i}\Pi_{\nu,i}\sin 2\chi_i)^2 + (\sum_i^{N_\nu} F_{\nu,i}\Pi_{\nu,i}\cos 2\chi_i)^2}}{\sum_i^{N_\nu} F_{\nu,i}}. \quad (1)$$

This implies that the *effective* number of emitting cells, at a given frequency, will depend upon the statistical distribution of the physical parameters of the cells in the system. From a statistical standpoint the *effective* number of emitting cells can be interpreted as the effective sample size (ESS) in a sample with weights (w_i), using the approach of [12]: ESS $= \frac{(\sum w_{\nu,i})^2}{\sum w_{\nu,i}^2}$, where the cell weights are defined as: $w_{\nu,i} = \frac{F_{\nu,i}}{\sum F_{\nu,i}}$, hence, the effective number of cells contributing to a given frequency, $N_\nu^{\rm eff}$, will read: $N_\nu^{\rm eff} = \frac{(\sum w_{\nu,i})^2}{\sum w_{\nu,i}^2} \leq N \rightarrow \kappa_\nu^{\rm eff} = \frac{1}{\sqrt{N_\nu^{\rm eff}}}$,and the average frequency-dependent fraction polarization will be: $\langle\Pi_\nu\rangle \approx \frac{<\Pi_\nu^{\rm ord}>}{\sqrt{N_\nu^{\rm eff}}} = \kappa_\nu^{\rm eff} < \Pi_\nu^{\rm ord} >$. The relevant result here is that since by definition $N \geq N_\nu^{\rm eff}$, then the fractional polarization, for a system with a significant dispersion on the cell fluxes, will have a lower fraction polarization compared to the case of almost identical cell fluxes:

$$\langle\Pi_\nu\rangle \approx \frac{< \Pi_\nu^{\rm ord} >}{\sqrt{N_\nu^{\rm eff}}} \geq \frac{< \Pi_\nu^{\rm ord} >}{\sqrt{N_\nu}} \quad (2)$$

3. Simulation setup and MC workflow

In a turbulent medium, even in the case of cells with comparable sizes, cells differ in their physical state. Most notably in the parameters of the electron energy distribution (EED), the Doppler (beaming) factor, the magnetic-field strength and orientation, and particle density. We therefore compute the synchrotron spectrum and polarization for each cell self-consistently, by generating the individual cell properties via a Monte Carlo approach. We assume that our system has a spherical geometry, with a characteristic radius, R_S, and that the single cell radius, $R_c \sim rR_S$, is distributed as a power-law via the scaling factor r, according to: $r \sim r^q, \quad q \leq 0, \quad 0 < r_{\rm min} < r < r_{\rm max}$. The EED is assumed to be a power-law with an exponential cut-off: $n(\gamma) = K\gamma^{-p}\exp(\gamma/\gamma_{\rm cut})$. The cell values of the magnetic field, B_c, of the beaming factor, δ_c, and of the EED index p_c, are distributed as a uniform PDF. We take into account four different scenarios for the PDF, $f_{\gamma_{\rm cut}}$, of $\gamma_{\rm cut}$, *fixed*:$f_{\gamma_{\rm cut}} = \gamma_{\rm cut}^{\rm ref}$, *uniform* : $f_{\gamma_{\rm cut}} = \mathcal{U}[\gamma_{\rm cut}^{\rm LB}, \gamma_{\rm cut}^{\rm ref}]$, *log-uniform* : $f_{\gamma_{\rm cut}} = \mathcal{U}[\log(\gamma_{\rm cut}^{\rm LB}), \log(\gamma_{\rm cut}^{\rm ref})]$, and a scenario establishing a linear relationship between R_c and $\gamma_{\rm cut}$, by setting $\gamma_{\rm cut}^{\rm min.ratio} = r_{\rm min}$ and

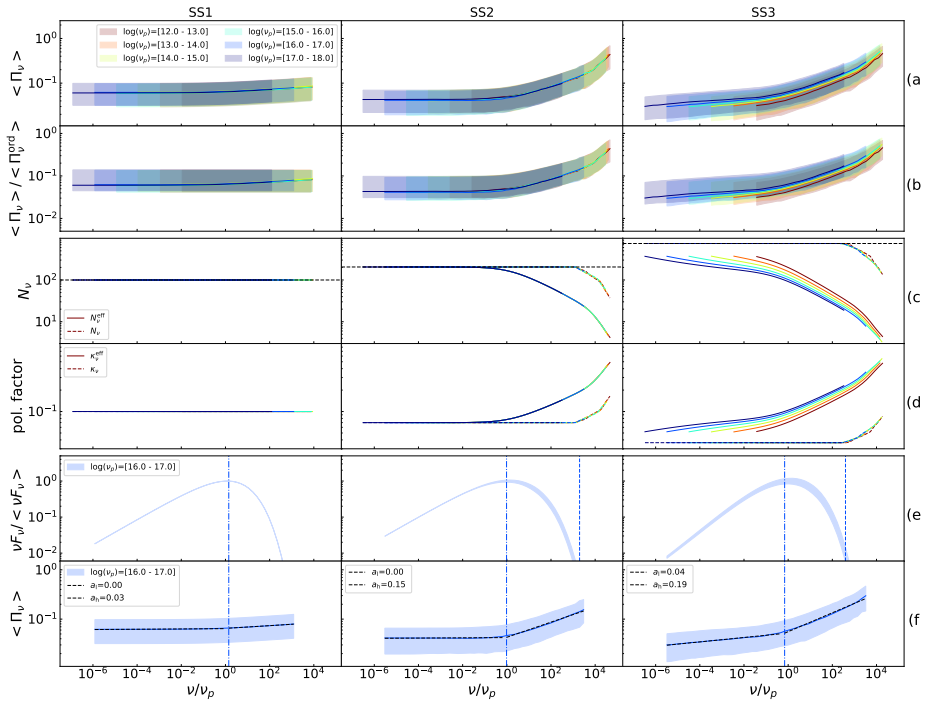

Figure 1: Different ν^p bins are marked by different colors, with the same color code for all the panels. *Top panels: Left column:* identical cells case (configuration SS1). *Middle column:* SS2 configuration, i.e. using $f_{\gamma_{\rm cut}}$=*log-uniform*. *Right column:* panel, SS3 configuration, same as SS2 but adding a flat PDF, for $p : f_p \sim \mathcal{U}[1.8, 2.8]$. All the trends are reported versus ν/ν_p. Solid lines mark the 0.5 quantiles, and the shaded areas mark the $1-\sigma$ quantiles dispersion for the MC trials. *Row a*: the trend of the ratio of $\langle\Pi_\nu\rangle$. *Row b*: same as for Row 1, but for trials-averaged trends for $\langle\Pi_\nu\rangle/\langle\Pi_\nu^{\rm ord}\rangle$. *Row c*: trials-averaged trends for N_ν (dashed lines) and $N_\nu^{\rm eff}$ (solid lines). *Row d*: trials-averaged trends for κ_ν (dashed line) and $\kappa_\nu^{\rm eff}$ (solid lines). *Row e*: SEDs for the ν_p bin =$[10^{16} - 10^{17}]$ Hz, the dashed vertical line the ν/ν_p marks value above which not all the cells contribute to the SED flux. The dot-dashed vertical lines mark $\nu = \nu_p^{\rm min}$, where $\nu_p^{\rm min}$ is the SED peak value for the lowest flux cell

$\gamma_{\rm cut}^{\rm ref} = r_{\rm max}$, and applying the transformation $\gamma_{\rm cut} \propto \gamma_{\rm cut}^{\rm ref} r$, leading to: $f_{\gamma_{\rm cut}} \propto \frac{\gamma_{\rm cut}^q}{(\gamma_{\rm cut}^{\rm ref})^{q+1}}$. We define the lower-bound for the randomization of $\gamma_{\rm cut}$, $\gamma_{\rm cut}^{\rm LB}$, as $\max(100, \gamma_{\rm cut}^{\rm ref}\gamma_{\rm cut}^{\rm min.ratio})$. The *linear* distribution is motivated by results from magnetic reconnection PIC simulations [8, 13], finding the EED high-energy cutoff scaling linearly with the plasmoids' width. All the distributions, except the *fixed* one, have a dispersion which is controlled by the value of $\gamma_{\rm cut}^{\rm min.ratio}$, with lower values of $\gamma_{\rm cut}^{\rm min.ratio}$ leading to larger values of the dispersion.

For each configuration of our MC, we run a calibration stage, that is, we calibrate N_c and $\gamma_{\rm cut}^{\rm ref}$, in order to get an optical polarization fraction,$\langle\Pi_\nu^{\rm opt}\rangle$, of about $[4-5]\%$ for the S SED peaking at $\nu_p^S = 1\times10^{17}$ Hz. As a reference value for the optical frequency, we use the value of 5×10^{14} Hz. At the end of the calibration stage, the same calibrated value of N_c is used for all the trials of a specific configuration, whilst the value of $\gamma_{\rm cut}^{\rm ref}$ is changed in order that ν_p^S samples six logarithmic bins in $[10^{12}$-$10^{18}]Hz$, for a total amount of 6000 trials per configuration. We consider two scenarios: one with cells of the same size (SS) and one with cell sizes distributed according to a power-law distribution (PL).

Table 1: The parameter space used for the PL distributed cell sizes MC scenario. For the magnetic field, the beaming factor, and magnetic field angle, we used the following PDFs: f_B=$\mathcal{U}[0.1, 1.0]$, f_δ=$\mathcal{U}[10, 30]$, and $f_{\chi^r_c}$=$\mathcal{U}[0, 2\pi]$. The total volume of the parameter space counts 780 different configurations.

PDF	Parameters	Values
f_{R_c}: PL	q	[0, –1.0, –1.5]
	$r_{\rm min}$	[0.01, 0.05, 0.1, 0.9]
	$r_{\rm max}$	1.0
f_{p_c}: $\mathcal{U}[p_0, p_0 + \Delta p]$	p_0	1.5
	Δ_p	[0.3,0.6,0.8,1.0,1.3,1.5]
$f_{\gamma_{\rm cut}}$: $\begin{cases}\delta_f\\ uniform\\ log\text{-}uniform\\ linear\end{cases}$	$\gamma_{\rm cut}^{\rm min.ratio}$	[0.01, 0.05, 0.1, 0.9]

4. MC results and comparison with observed data

We begin by investigating the SS scenario, with three different configurations: SS1, with $f_{\gamma_{\rm cut}}$=*fixed* and $p_c = 2.3$, SS2, same as SS1 but using $f_{\gamma_{\rm cut}}$=*log-uniform*, and finally, the SS3 configuration, same as for SS2, but adding a uniform PDF, for p, $f_p \sim \mathcal{U}[1.8, 2.8]$, For all the three configurations, we use $q = 0$, $r_{\rm min} = r_{\rm max} = 0.1$, $B = 0.1$, $\delta = 10$, $\gamma_{\rm cut}^{\rm min.ratio} = 0.1$, and we perform 1000 trials. In Figure 1 we show the impact on the frequency-dependent polarization pattern $\langle\Pi_\nu\rangle$, for different level of randomization, going from configuration SS1 to SS3. The trends for $\langle\Pi_\nu\rangle$ and $\langle\Pi_\nu\rangle/\langle\Pi_\nu^{\rm ord}\rangle$are shown in the panels of row a and b, respectively. The different colors identify the ν^p bins, and are the same for all the panels. The c-row panel shows the trends for the trials-averaged value of $N_\nu^{\rm eff}$, and the d-row panels the trials-averaged trends for the depolarization factor κ_ν (dashed line) and $\kappa_\nu^{\rm eff}$ (solid lines). The SEDs for the case ν_p bin =$[10^{16} - 10^{17}]$ Hz are represented in the row e panels (the shaded area encompasses the entire MC range). It is evident that for the case of identical cells (SS1), N_ν and $N_\nu^{\rm eff}$ coincide, and this translates to $\kappa_\nu = \kappa_\nu^{\rm eff}$. On the contrary, by adding a randomization on $\gamma_{\rm cut}$ (middle column,SS2), we start to introduce a modulation on $N_\nu^{\rm eff}$, with $N_\nu^{\rm eff} < N_\nu$ for $\nu \geq \nu_p^{\rm min}$, leading to a difference between the depolarization factor with $\kappa_\nu^{\rm eff} > \kappa_\nu$, for $\nu \geq \nu_p^{\rm min}$. This modulation is not only related to the fact that above a given $\gamma_{\rm cut}$ only a few cells are contributing, but mostly to the different cells flux contribution, which is shown by the $\kappa_\nu^{\rm eff}$ trend. This modulation introduces a broken power-law trend in $N_\nu^{\rm eff}$ and consequently in $\kappa_\nu^{\rm eff}$ and $\langle\Pi_\nu\rangle$, with at turnover point around $\nu \geq \nu_p^{\rm min}$. The turnover still persists when we also introduce randomization on p (left column,SS3). We analyze the low (a_l) and high-energy (a_h) indices of the $\langle\Pi_\nu\rangle$ polarization pattern, and we focus on the bin ν_p bin =$[10^{16} - 10^{17}]$ (rows e and f of Figure 1), and we find that the a_h trends remain consistent across all configurations (expect the SS1 and SSH1 configurations), indicating that the high-frequency polarization slope is primarily influenced by the modulation of $N_\nu^{\rm eff}$ due to the dispersion in $\gamma_{\rm cut}$. On the other hand, the low-frequency slope a_l is significantly increased by the dispersion on p.

4.1 IXPE HPS $\langle\Pi_\nu\rangle$ trends

To compare the Π_ν trends observed in IXPE multiwavelength campaigns to our simulations, we perform the same analysis as described for the SS scenario, but using the PL cells size scenario, summarized in Table 1. In place of a_l and a_h, we evaluate $a_{\rm mm-o}$ and of $a_{\rm o-X}$, respectively. The reference values used for the mm, optical, and X-ray frequencies are 2×10^{11} Hz, 5×10^{14} Hz, and 1×10^{18} Hz, respectively. The shaded areas in Figure 2, represent the ±20% boundary for the

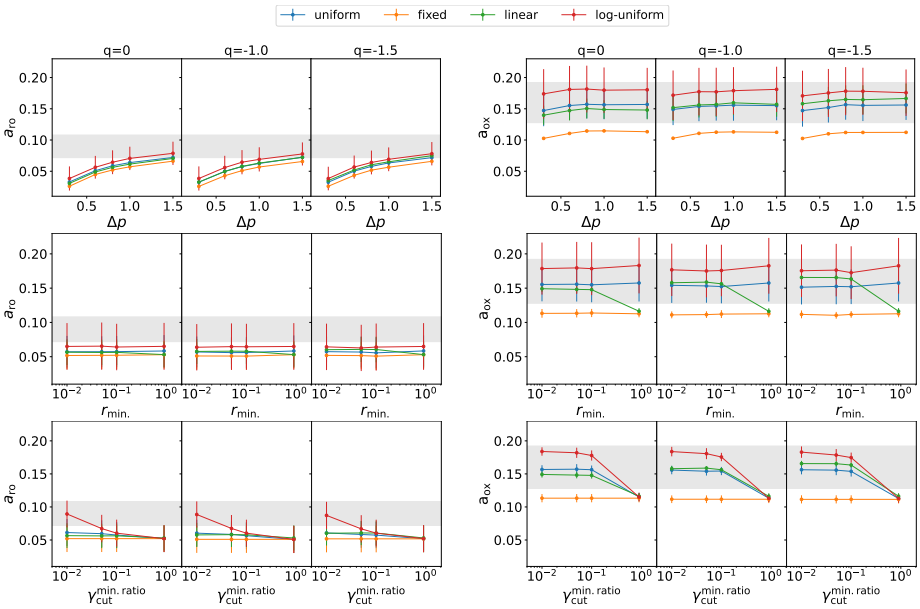

Figure 2: Summary of polarization slope trends for power-law distributed cell sizes. *Top panels:* Low-energy (a_l, left) and high-energy (a_h, right) polarization slopes as a function of the dispersion in the electron energy distribution index, Δ_p. *Middle panels:* a_l and a_h as a function of the minimum cell size ratio, $r_{\rm min}$. *Bottom panels:* a_l and a_h as a function of the minimum cutoff ratio, $\gamma_{\rm cut}^{\rm min.ratio}$

observed HSP IXPE multiwavelength campaigns values of $a_{\rm mm-o}$ and of $a_{\rm o-X}$, and the solid lines, represent the results of our MC simulations, binned for the HSPs, with ν_p^S in $[10\times15-10\times18]$ Hz. Consistently with the case SS case, we find that the most relevant parameters for $a_{\rm mm-o}$ are the dispersion in p, which is positively correlated with $a_{\rm mm-o}$, and the value of $\gamma_{\rm cut}^{\rm min.ratio}$, which has a negative correlation, for the *log-uniform* $f_{\gamma_{\rm cut}}$. In general, the observed data favor a dispersion $\Delta_p \gtrapprox 1$, and values of $\gamma_{\rm cut}^{\rm min.ratio} \lessapprox 0.1$ for the *log-uniform* distribution. We also notice that *log-uniform* distribution provides the best match with the data. The IXPE values of $a_{\rm o-X}$ provide a lower constraining power, indeed, all the $f_{\gamma_{\rm cut}}$ distributions, except the *fixed* one, are compatible with the observations, for the entire parameter space. Anyhow, a significant tension with the data is observed for $r_{\rm min}\approx 1$, for the case of *linear* $f_{\gamma_{\rm cut}}$, and for values of $\gamma_{\rm cut}^{\rm min.ratio}\approx 1$, for all the $f_{\gamma_{\rm cut}}$ distributions.

4.2 RoboPol trends.

To test if our MC samples are statistically compatible with the RoboPol observed trend, we use a two-dimensional two-sample Kolmogorov–Smirnov (KS) test, where the two independent variables are ν_p^S and $\Pi_{\rm opt}$ (evaluated at 5×10^{14} Hz). In Figure 3 we show the trends of the KS test p-value as a function of Δ_p (top panels), $r_{\rm min}$ (middle panels), and $\gamma_{\rm cut}^{\rm min.ratio}$ (bottom panels). We notice that, consistently with the HSPs IXPE trend, the RoboPol $\Pi_{\rm opt}$-vs-ν_p^S trend rules out the *fixed* $f_{\gamma_{\rm cut}}$ PDF, and disfavor values of $\gamma_{\rm cut}^{\rm min.ratio}\gtrapprox 0.1$, for all the $f_{\gamma_{\rm cut}}$ PDFs, and values of $r_{\rm min}\gtrapprox 0.1$ for the *linear* $f_{\gamma_{\rm cut}}$. Anyhow, the $\Pi_{\rm opt}$-vs-ν_p^S trend does not constrain the dispersion Δ_p. The reason for this behavior stems from the fact that the observed RoboPol $\Pi_{\rm opt}$-vs-ν_p^S trend depends mostly on the 'distance' between the optical frequency and ν_p^S, and in particular from the modulation of

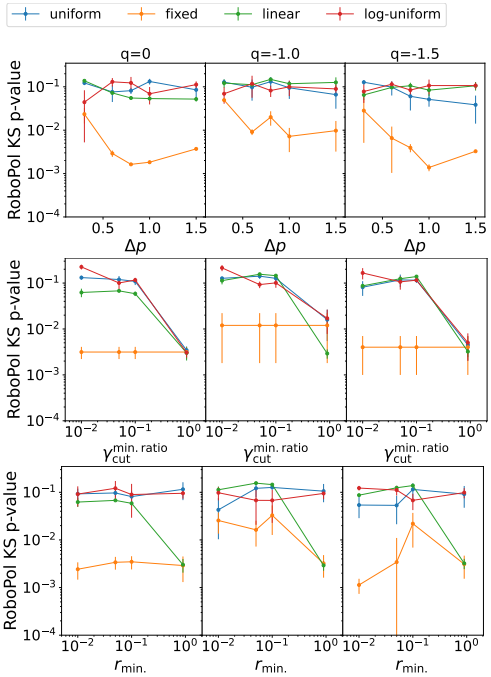

Figure 3: KS test p-value trends as a function of Δ_p (top panels), $r_{\rm min}$ (middle panels), and $\gamma_{\rm cut}^{\rm min.ratio}$ (bottom panels). The left, middle, and right columns refer to the selected values of q, equation to 0, 1, and -1.5, respectively. The dashed horizontal lines mark the 0.05 p-value

$N_\nu^{\rm eff}$, and consequently of the polarization factor, $\kappa_\nu^{\rm eff}$, below ν_p^S. Finally, in Figure 4 we plot the best runs for three different $f_{\gamma_{\rm cut}}$ PDFs: *uniform, log-uniform* and *linear*. The left panels show the $\Pi_{\rm opt}$-vs-ν_p^S trends for both the MC simulations and the observed RoboPol data, the center panels show the trends of the dispersion of the MC optical EVAP angle, $\sigma_\chi^{\rm opt}$ vs ν_p^S, and the right panels, the IXPE HPS observed trends for the IXPE compared to the MC results, extracted from the same runs used for the RoboPol panels. The decreasing trend of the optical EVAP angle dispersion, has the same root of the $\Pi_{\rm opt}$-vs-ν_p^S. i.e. the modulation of $N_\nu^{\rm eff}$ below ν_p^S, for lower values of ν_p^S, the optical $N_\nu^{\rm eff}$ decreases, hence, the dispersion on the optical EVAP angle increases.

5. Discussion and conclusions

We have presented an analysis of the multiwavelength patterns of Π_ν of blazars, based on a comprehensive Monte Carlo, implementing spatially resolved emitting regions, with distinct physical properties, in a purely turbulent framework, testing different levels of correlation between the size of the cells, and cut-off in the electron distribution. The results demonstrate that a minimal, turbulence-driven multi-zone scenario can account for the key features seen in both IXPE and RoboPol datasets, showing that the best agreement is obtained for models with a broad dispersion in the EED index ($\Delta_p \gtrsim 0.6$) and values of $\gamma_{\rm cut}^{\rm min.ratio} \lesssim 0.1$ (that is, a large dispersion on $\gamma_{\rm cut}$), with the *log-uniform* $f_{\gamma_{\rm cut}}$ distribution providing the best agreement. We also notice that the *linear* model, does not provide statistical improvement compared to the *log-uniform*, hence the current dataset and analysis are not able to find a piece of significant evidence for this model, which mimics statistically the magnetic reconnection scenario. We stress that our model does not test the presence

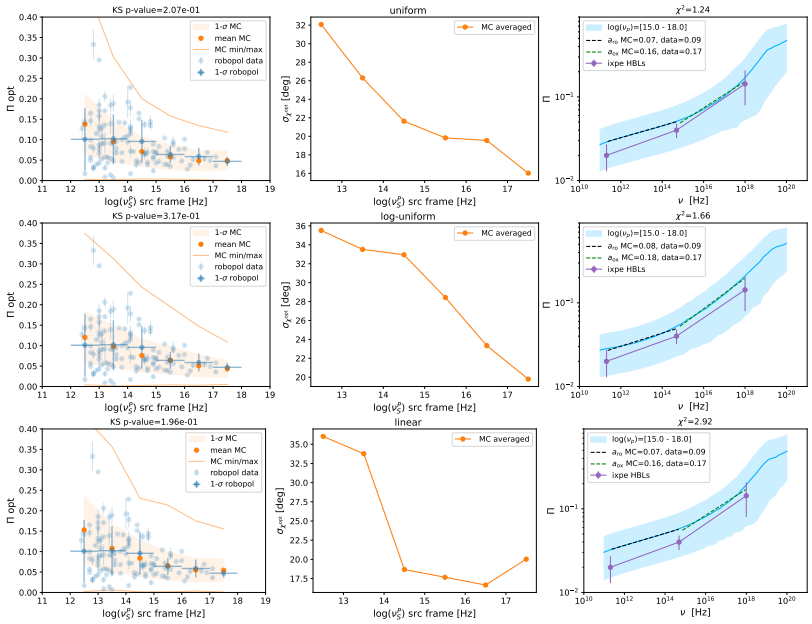

Figure 4: The best runs for tree different $f_{\gamma_{\rm cut}}$: *uniform, log-uniform*, and *linear*. The left panels show the $\langle \Pi_\nu^{\rm opt} \rangle$ trends for both the MC simulations and the observed RoboPol data, the center panels show the trends of the MC-averaged dispersion of the MC optical EVAP vs ν_p^S, and the right panels show the IXPE HPS observed trends compared to the MC results extracted from the same runs used for the RoboPol panels.

of a shock and that the investigation on the dispersion of the optical EVPA is limited to the multi-zone scenario, with no implications on the observed systematci rotations at different wavelengths. Hence, our analysis could fit a purely stochastic scenario or a scenario where the turbulent medium develops within the shock. In this regard, we notice how HSP, such as Mrk 421 have shown in their spectral shapes evidence for the coexistence of both first-order shock acceleration and stochastic acceleration [16, 17].

References

[1] Abdo A. A., Ackermann M., Agudo I., et al., 2010, ApJ, 716, 30
[2] Angelakis E., et al., 2016, Monthly Notices of the Royal Astronomical Society, 463, 3365
[3] Blandford R. D., Königl A., 1979, The Astrophysical Journal, 232, 34
[4] Blandford R. D., Rees M. J., 1978, Proceedings of the Pittsburgh Conference on BL Lac Objects, pp 328–341
[5] Böttcher M., Reimer A., Sweeney K., Prakash A., 2013, The Astrophysical Journal, 768, 54
[6] Di Gesu L., Marshall H. L., Ehlert S. R., et al., 2023, ApJL, 949, L42
[7] Kouch P. M., et al., 2024, , 689, A119
[8] Li X., Guo F., Liu Y.-H., Li H., 2023, ApJ , 954, L37
[9] Liodakis I., et al., 2022, Nature , 611, 677
[10] Marscher A. P., Jorstad S. G., 2022, Universe, 8, 644
[11] Rybicki G. B., Lightman A. P., 1986, in , Radiative processes in astrophysics
[12] Shook-Sa B. E., Hudgens M. G., 2020, arXiv: Applications
[13] Sironi L., Giannios D., Petropoulou M., 2016, MNRAS , 462, 48
[14] Tramacere A., 2020, JetSeT: Numerical modeling and SED fitting tool for relativistic jets, Astrophysics Source Code Library, record ascl:2009.001
[15] Tramacere A., 2025, arXiv:2510.05324
[16] Tramacere A., Giommi P., Perri M., Verrecchia F., Tosti G., 2009, , 501, 879
[17] Tramacere A., Massaro E., Taylor A. M., 2011, ApJ , 739, 66
[18] Weisskopf M. C., Ramsey B., O'Dell S., et al., 2022, JATIS, 8, 026002
[19] Westfold K. C., 1959, ApJ , 130, 241